Solar Physics (2023) 298:89
https://doi.org/10.1007/s11207-023-02176-9

RESEARCH

Distributions of Mesoscale Periodic Structures in the Elemental and Ionic Composition of the Solar Wind

Irena Gershkovich[1] · Susan Lepri[1] · Nicholeen Viall[2] · Simone Di Matteo[2,3] · Larry Kepko[2]

Received: 21 March 2023 / Accepted: 1 June 2023 / Published online: 17 July 2023

Abstract

Multiple statistical and event studies based on *in situ* observations have shown that the solar wind contains mesoscale (∼ 100 – 10,000 Mm) periodic structures in the proton number density. Remote observations of such structures and event studies of concurrent variations in composition have demonstrated that they can form in the solar atmosphere and be preserved while advecting outwards through the heliosphere. Viall, Kepko, and Spence (*J. Geophys. Res. (Space Phys.)* **113**, A07101, 2008; *J. Geophys. Res. (Space Phys.)* **114**, A01201, 2009) and Kepko, Viall, and Wolfinger (*J. Geophys. Res. (Space Phys.)* **125**(8), e28037, 2020) have reported that periodic proton density structures preferentially occur at specific radial length scales and have published their distributions from Wind measurements near L1. Here, we conduct a statistical study of 14 years (1998 – 2011) of 12-minute composition data measured by the Solar Wind Ion Composition Spectrometer instrument aboard the Advanced Composition Explorer spacecraft. We found that the elemental and ionic composition also contain statistically significant mesoscale periodic structures and, for the first time, present occurrence distributions for elemental abundance ratios with low, intermediate, and high first ionization potentials as well as for key solar wind charge states. These distributions set important constraints on solar wind formation in general and the formation of periodic mesoscale solar wind structures specifically, as the elemental and ionic composition are known to be determined at the Sun and to not evolve during advection.

✉ I. Gershkovich
igershko@umich.edu

S. Lepri
slepri@umich.edu

N. Viall
nicholeen.m.viall@nasa.gov

S. Di Matteo
simone.dimatteo@nasa.gov

L. Kepko
larry.kepko@nasa.gov

1 The University of Michigan, Ann Arbor, MI 48109, USA

2 NASA - Goddard Space Flight Center, Greenbelt, MD 20771, USA

3 The Catholic University of America, Washington, DC 20664, USA

Keywords Solar wind · Plasma astrophysics · Heliosphere · Stellar atmospheres

1. Introduction

In this work, we present the results of a statistical study of periodic variations that have previously been observed in event studies of the ionic and elemental composition of the solar wind (Kepko et al., 2016; Viall, Kepko, and Spence, 2009; Gershkovich et al., 2022). Composition is a particularly important tracer of solar wind formation as variations in the elemental composition and charge state are established in the solar atmosphere and do not evolve en route to the point of observation. This is due to processes occurring in different regions of the Sun producing different elemental and ion fractionations that are preserved as the plasma is expelled at supersonic speeds (Ogilvie et al., 1980), resulting in the collisionless nature of the solar wind beyond the freeze-in radius of $\sim 1.1-4\ R_s$, depending on the element (Hundhausen, Gilbert, and Bame, 1968; Landi et al., 2012).

In situ observations of the solar wind have shown that it is not laminar but instead highly structured at a variety of scales (Viall, DeForest, and Kepko, 2021; Verscharen, Klein, and Maruca, 2019). These scales range from 1 – 2 minute magnetic holes (Winterhalter et al., 1994) to very large-scale structures such as coronal mass ejections and stream interaction regions (Kilpua, Koskinen, and Pulkkinen, 2017; Richardson, 2018). On mesoscales that are larger than kinetic scales but smaller than the largest structures in the solar wind ($\sim 100-10{,}000$ Mm or, alternatively, on timescales of several minutes to several hours), some structures enter the solar wind during formation in the solar atmosphere, while others evolve during propagation through the heliosphere. The structures that enter the solar wind directly at the Sun and persist until they are measured retain key information about the processes that form the solar wind. Mesoscale structures not only capture signatures of solar wind formation but are also significant because they can drive magnetosphere dynamics (Viall, DeForest, and Kepko, 2021) and shape the medium through which large-space weather events propagate. Structures at these scales have been observed in Solar Terrestrial Relations Observatory (STEREO) white light remote images down to the resolution of the instrument (DeForest et al., 2016, 2018). Magnetic flux rope structures as small as 50 Mm (Murphy et al., 2020) have been detected *in situ,* and structures in plasma density have been observed at scales ranging from 50 to 2000 Mm (Stansby and Horbury, 2018). Mesoscale structures have also been identified in combinations of plasma and magnetic signatures (Borovsky, 2008; Di Matteo et al., 2019; Rouillard et al., 2010, 2020; Sanchez-Diaz et al., 2019).

Quasi-periodic proton density structures (PDSs) are a subset of mesoscale structures observed in the solar wind. These were first discovered in event studies that showed a direct relationship between mHz-range magnetic oscillations in the magnetosphere (several minute to several hour temporal scales) and discrete frequencies in the upstream solar wind density (Kepko, Spence, and Singer, 2002; Kepko and Spence, 2003). Multiple event studies have shown that there are direct links between periodic structures observed in solar wind proton number density and periodicities in the magnetosphere in radar (Fenrich and Waters, 2008), ionospheric (Dyrud et al., 2008) and ground magnetometer (Villante et al., 2007; Villante, Di Matteo, and Piersanti, 2016) data at frequencies ranging from ~ 0.2 mHz to ~ 4 mHz. Viall, Kepko, and Spence (2009) found similar statistically significant enhancements, ranging from ~ 0.5 mHz to ~ 4 mHz, observed in 11 years of Wind proton density data, measured near Lagrange point 1 (L1), as well as in dayside Geostationary Operational Environmental Satellites (GOES) magnetometer data.

Since the initial discovery of periodic density structures in the solar wind, there have been efforts to categorize them and identify their sources. Viall, Kepko, and Spence (2008), Viall, Kepko, and Spence (2009) and Kepko, Viall, and Wolfinger (2020) reported statistically significant bands of periodic structures in *in situ* solar wind proton density measurements. Viall and Vourlidas (2015) also reported on a statistical study of periodic structures found in coronagraph data. These structures exhibit a characteristic scale such that certain periodicities occur more than others during the observational period and therefore cannot simply be attributed to turbulence. Several lines of evidence indicate that periodic variations carry signatures of solar wind formation processes. *In situ* measurements of composition, magnetic field and strahl pitch angle variations point to magnetic reconnection events that could only have originated at the Sun during solar wind release and acceleration (Kepko et al., 2016; Di Matteo et al., 2019; Viall, Kepko, and Spence, 2009). Anisotropic temperature changes were found within PDSs that were not observed near L1 in Helios data by Di Matteo et al. (2019). These results are consistent with formation in the solar atmosphere and temperature isotropization in transit. PDSs identified in STEREO/Sun Earth Connection Coronal and Heliospheric Investigation (SECCHI) white light image data are found at distances as close to the Sun as 2.5 R_s and are observed to accelerate with the surrounding solar wind (DeForest et al., 2016, 2018; Viall and Vourlidas, 2015; Viall et al., 2010). Rouillard et al. (2020) tracked large streamer blobs containing approximately hour-long sub-structures from STEREO/SECCHI to their arrival at the Parker Solar Probe, thus linking periodic structures observed in images to *in situ* observations. The above findings show that the solar wind is often formed and released via quasi-periodic mesoscale density structures and highlight the importance of extending the statistical studies of such structures to properties of the solar wind, such as its composition.

In this analysis, we move beyond statistical studies of proton density structures to studies of periodic density structures observed in the charge states and elemental composition of the solar wind, measured at L1 by the Solar Wind Ion Composition Spectrometer aboard the Advanced Composition Explorer spacecraft (ACE/SWICS) at its native 12-minute resolution. For the first time, we provide occurrence distributions of statistically significant frequencies found in the relative abundances of elements with low first ionization potential (FIP), intermediate-FIP, high-FIP as well as in the charge state. These are particularly relevant, as the elemental composition and charge state are determined in the solar atmosphere and do not evolve as the solar wind advects through the heliosphere, thus providing important constraints on the processes that govern solar wind formation.

Different types of regions on the Sun have distinct compositions and charge-state signatures. In particular, active regions (ARs) and Quiet Sun (QS) regions are known to have enhanced low-FIP abundances and higher charge states than coronal hole (CH) regions (Viall and Borovsky, 2020). The solar wind charge states are determined in the solar atmosphere within several solar radii of the Sun; as the solar wind plasma expands into the heliosphere, the interaction cross sections become too low to influence the plasma, and the charge states of individual ions freeze in and stop evolving (Gloeckler, Zurbuchen, and Geiss, 2003; Landi et al., 2012). The elemental composition, on the other hand, is determined in the chromosphere, predominantly by ponderomotive forces (Laming, 2015; Laming et al., 2019) and also stops evolving after the release of a given parcel of solar wind. The FIP-dependent abundances and the solar wind charge states often vary together on long terms and in a global sense, but not always, due the different physics involved (Stakhiv et al., 2015). The similarities, as well as the differences in the variation of these two diagnostics, can provide information about the sources of the solar wind and the processes involved in its release.

Mesoscale periodic structures are thought to be imprinted onto the solar wind through interchange reconnection (Fisk, 2003; Antiochos et al., 2011; Crooker, Gosling, and Kahler,

2002; Kepko et al., 2016; Viall, Spence, and Kasper, 2009; Réville et al., 2020; Di Matteo et al., 2019; Viall and Vourlidas, 2015; Higginson and Lynch, 2018) between closed and open magnetic field lines. By this mechanism, plasma parcels from closed AR and QS regions can periodically enter the flow of solar wind along open magnetic-field lines emanating from CH regions. These variations are, as previously stated, preserved during propagation and measured by *in situ* instruments such as ACE/SWICS. The mechanisms associated with the periodicity of these reconnections are an active area of research and not yet fully understood. However, the elemental and charge state composition occurrence distributions of significant frequencies that we present here provide important constraints on the nature of these processes.

Our distributions cover a frequency range between ~ 0.1 mHz to ~ 0.7 mHz, near the lower bound of the periodic proton density structures identified by previous studies at L1 due to the longer 12-minute native resolution of the ACE/SWICS instrument. This study covers a time span of 14 years (1998 – 2011) and explores the impact of solar cycle dependencies on the periodicities identified. We find statistically significant periodic enhancements in the composition data, and that these enhancements occur more at some frequencies than others, thus exhibiting a characteristic scale.

Thus far, we have given an overview of prior studies that have reported and catalogued mesoscale periodic structures, primarily in the proton number density of the solar wind, and have motivated the need for further studies, particularly statistical studies such as the one we present here, focusing on the solar wind elemental and ionic composition. In Section 2, we provide an overview of the methodology used and discuss relevant aspects of the ACE/SWICS instrument. We provide the resulting occurrence distributions and show the dependence of our results on solar activity in Section 3. In Section 4, we discuss these results and provide a summary chart that synthesizes the findings for different composition ratios and solar wind activity levels. Finally, in Section 5, we summarize the significance of our findings and provide plans for future work.

2. Methods

2.1. Study Overview

We have prepared and validated 14 years (1998 – 2011) of ACE/SWICS heavy ion composition time series data in order to conduct a statistical study of the mesoscale periodic structures that it contains. Fundamentally, we used a similar spectral analysis technique to what was used for statistical studies of proton density structures (Kepko, Viall, and Wolfinger, 2020; Viall, Kepko, and Spence, 2008). We analyze charge state abundance ratios (O^{7+}/O^{6+} and C^{6+}/C^{4+}), low-FIP (Fe/O, Mg/O and Si/O), intermediate-FIP (C/O and S/O) and high-FIP (He/O) relative abundance values in order to compare and contrast their distributions of mesoscale periodic structure occurrences. All available charge states were integrated over in order to construct the low-FIP, intermediate-FIP and high-FIP abundance ratios.

The 14-year dataset was partitioned using 24-hour segment lengths. Each segment was prepared according to the criteria given in Gershkovich et al. (2022) and briefly summarized in this section. As in that work, we chose 24-hour window lengths in order to ensure that we had enough data points (120) to run spectral analysis with sufficient spectral resolution and apply five orthogonal Slepian data tapers (Slepian, 1978). For this analysis, we have set the following minimum requirements to ensure that each segment analyzed for periodicity has sufficient continuity and counts: (i) We require that the percentage of missing data

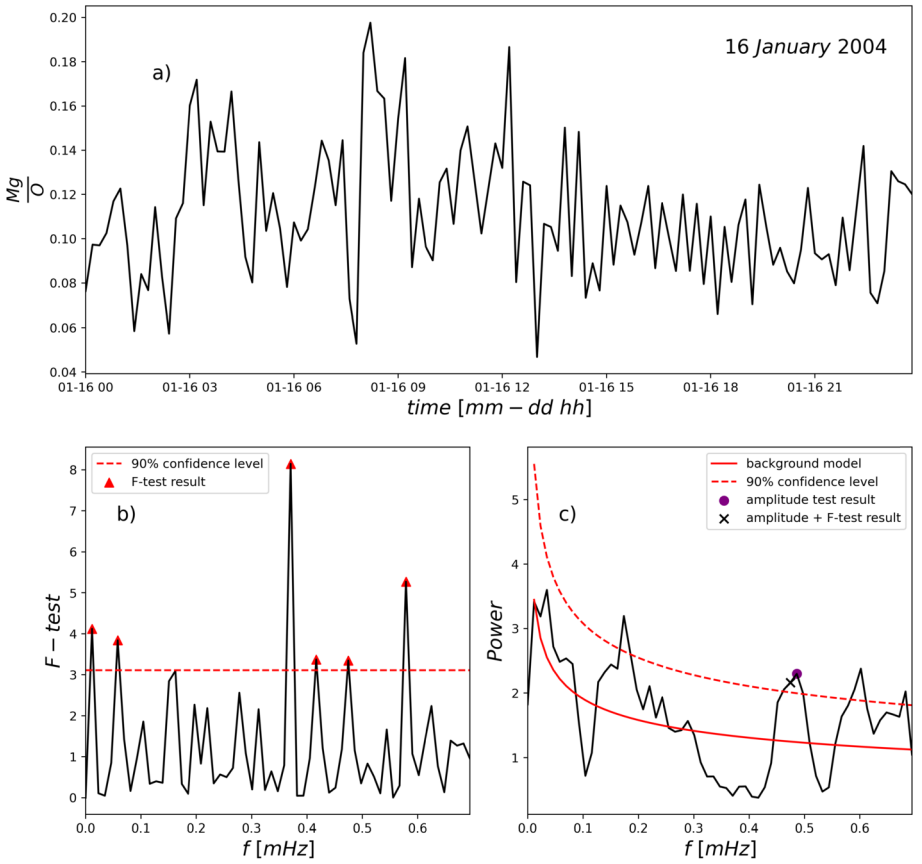

Figure 1 Time series and spectral analysis results for the Mg/O 24-hour segment beginning on 2004-01-16 00:00:00 UT. Panel (a) shows the Mg/O abundance ratio as a time series. Panel (b) shows the F-test signals as red triangles, above the dashed red 90% confidence level line. Panel (c) shows the estimated power spectral density in black, the background fit as a solid red line and the 90% confidence level as a dashed red curve. Results that passed the amplitude test are marked by purple circles. Results that pass both the amplitude and F-test are marked by a black "x". The ∼0.5 mHz peak passes the amplitude test and the F-test at a 90% confidence level.

points must not exceed 20% for each segment. (ii) The number of allowed missing data points in a row must be less than 3. (iii) We required a minimum of 25 instrument counts for each data point in the time series to be validated. These criteria must be met for all segments and ratios included in the study in order to ensure that physical variations are properly represented, such that spectral analysis produces robust and accurate results. Furthermore, we split the resulting frequency occurrence distributions into groups by solar activity (with years selected for high, medium, and low average sunspot numbers) in order to determine the effect of solar activity on the number (normalized to the number of segments that we could validate for that category) and values of the periodic structures identified.

We used the spectral analysis technique developed by Di Matteo, Viall, and Kepko (2021) based on the multitaper method (Thomson, 1982). This technique employs an F-test, identifying phase-coherent periodicities, and an amplitude test, testing for power enhancements relative to a background spectrum estimated by robustly fitting a bending power law model

via a maximum-likelihood procedure. We apply the technique with a time-halfbandwidth product (NW) equal to 3 corresponding to an effective spectral resolution of $6 f_{\mathrm{Ray}}$ (the Rayleigh frequency, the inverse of the product of the number of data points in each 24-hour time series (N) and their separation in time (t): $f_{\mathrm{Ray}} = \frac{1}{N\delta t}$). Finally, we require that each segment passes the harmonic F-test and the amplitude test (Gershkovich et al., 2022; Di Matteo, Viall, and Kepko, 2021) at a 90% confidence level.

The time series and spectral analysis results for an example Mg/O 24-hour segment, analyzed as part of this statistical study, are shown in Figure 1 for illustrative purposes. Spectral analysis reveals frequency components that are present, but are often not apparent when examining a time series plot by eye. Panel (a) shows the Mg/O abundance ratio as a time series. Panel (b) shows the F-test signals as red triangles above the dashed red 90% confidence level line. Panel (c) shows the estimated power spectral density in black, the background fit as a solid red line, and the 90% confidence level as a dashed red curve. Results that passed the amplitude test are marked by purple circles. Results that pass both the amplitude and F-test are marked by a black "x". The ~ 0.5 mHz peak passes the amplitude test and the F-test at a 90% confidence level. Thousands of such segments were analyzed as part of this work, and the results are presented as occurrence distributions for each abundance and charge state ratio in the next section.

2.2. Instrument Description

The ACE mission has been operating continuously since 1998. ACE orbits L1 and onboard is the SWICS instrument – a plasma composition spectrometer focused on measuring the distributions of heavy ions in the solar wind. The ACE/SWICS spectrometer is identical to the SWICS instrument flown as part of the Ulysses mission (Gloeckler et al., 1992, 1998). It is a triple coincidence time-of-flight mass spectrometer that contains an electro-static analyzer (ESA) at its entrance to select ions with specific energy-per-charge values as well as a time-of-flight (TOF) telescope with integrated micro-channel plates (MCPs) and solid-state detectors (SSDs). The combination of the TOF telescope and the ESA allows for the calculation of an ion's mass, charge, and speed by measuring both its energy and time of flight. This produces the most robust measurements of heavy ion distributions within the instrument's native 12-minute resolution limits. The SWICS instrument has made substantial contributions to our understanding of the properties and composition of the solar wind. It has discovered most of the known pickup ions in the heliosphere (Gloeckler et al., 1993; Geiss et al., 1995; Gloeckler et al., 2000; Von Steiger et al., 2000) as well as helped distinguish the broad properties of the fast ($V > 500$ km s^{-1}) and slow ($V < 500$ km s^{-1}) solar wind categories (Von Steiger et al., 2000), which are now known to originate from different solar source regions. The instrument as well as the data processing method employed to extract distributions have been described in detail in previous work (Gloeckler et al., 1992, 1998; Von Steiger et al., 2000; Shearer et al., 2014). Most studies with ACE/SWICS have used data summed to a 2-hour time resolution. Here, however, we used the native 12-minute resolution of the instrument to study smaller structures in the solar wind at "meso" scales (as was also done by Gershkovich et al. (2022) and Kepko et al. (2016)).

3. Results

3.1. Distributions: Statistical Significance and Characteristic Scale

We prepared and ran all segments of the 1998 – 2011 ACE/SWICS data according to the analysis procedure described in Section 2.1. Figures 2, 3, 4, 5 show the resulting occurrence

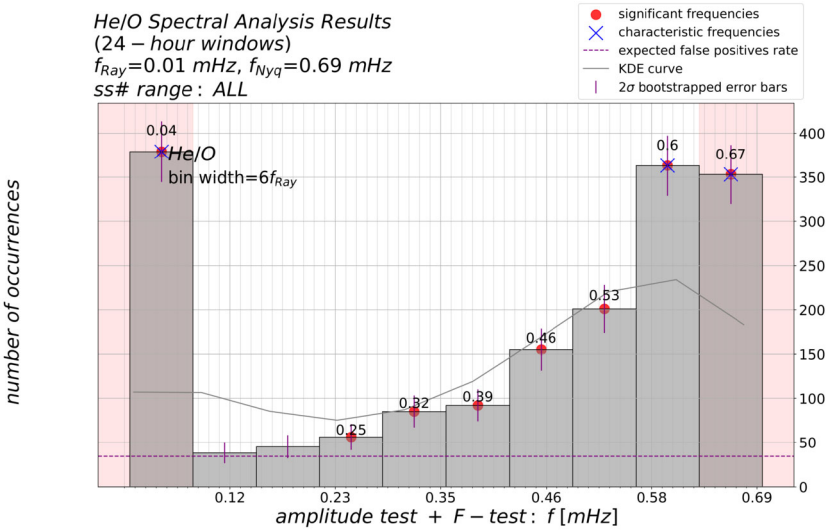

Figure 2 Periodic density structure occurrence distribution for the high-FIP He/O abundance ratio. Error bars showing 2σ of the bootstrapped distribution are plotted as solid purple vertical lines. The occurrence distribution is shown in gray, and the expected false-positive rate for the method is shown as a dotted purple horizontal line. Significant frequencies are defined to rise $\geq 2\sigma$ above the expected false-positive rate. These are marked on the plot by red dots and the numerical value of the corresponding bin center. Characteristic frequencies are defined to rise $\geq 1\sigma$ above the gray KDE curve and are marked with a blue "x". The extreme low- and high-frequency ranges shaded in red on each plot indicate frequency bins prone to false positives, according to Monte-Carlo simulations (Di Matteo, Viall, and Kepko, 2021), and are therefore not considered statistically significant results.

distributions for the charge state, low-FIP, intermediate-FIP, and high-FIP abundance ratios with a bin width of $6\,f_{\mathrm{Ray}}$. This is the maximum effective resolution of this method with five applied tapers. These distributions were computed with the data for all categories of solar activity (and the full dataset). Each ratio is shown in its own panel within each figure. The dotted horizontal line in each panel indicates the expected false-positive rate of the combined amplitude test and harmonic F-test for that distribution, with each test passing at the 90% confidence level (Di Matteo, Viall, and Kepko, 2021; Gershkovich et al., 2022). The extreme low- and high-frequency ranges shaded in red on each plot indicate frequency bins prone to false positives according to Monte-Carlo simulations based on the bending power law (BPL) background assumption (Di Matteo, Viall, and Kepko, 2021) and are therefore not considered statistically significant results. The error bars on the distributions are estimated by bootstrapping (Efron and Tibshirani, 1994) and indicate a deviation of 2σ. Statistically significant enhancements in the occurrence distributions are labeled in black with their numerical values in units of mHz; we required these to rise $\geq 2\sigma$ above the line designating the expected false positives rate of the spectral analysis method. The black curve in each panel is the kernel density estimation (KDE) to the distribution computed using a Gaussian Kernel. We used "Scott's rule" (Scott, 2015) to select the bandwidth parameter. Points that rise 1σ above the KDE estimator are marked with a blue "x" and considered to indicate that a characteristic scale is present, meaning that certain frequencies are enhanced relative to the overall distribution shape.

Figure 2 shows an all-year distribution for He/O that rises at an increasing rate with frequency. The statistically significant frequency band (i.e., frequencies rising 2σ above

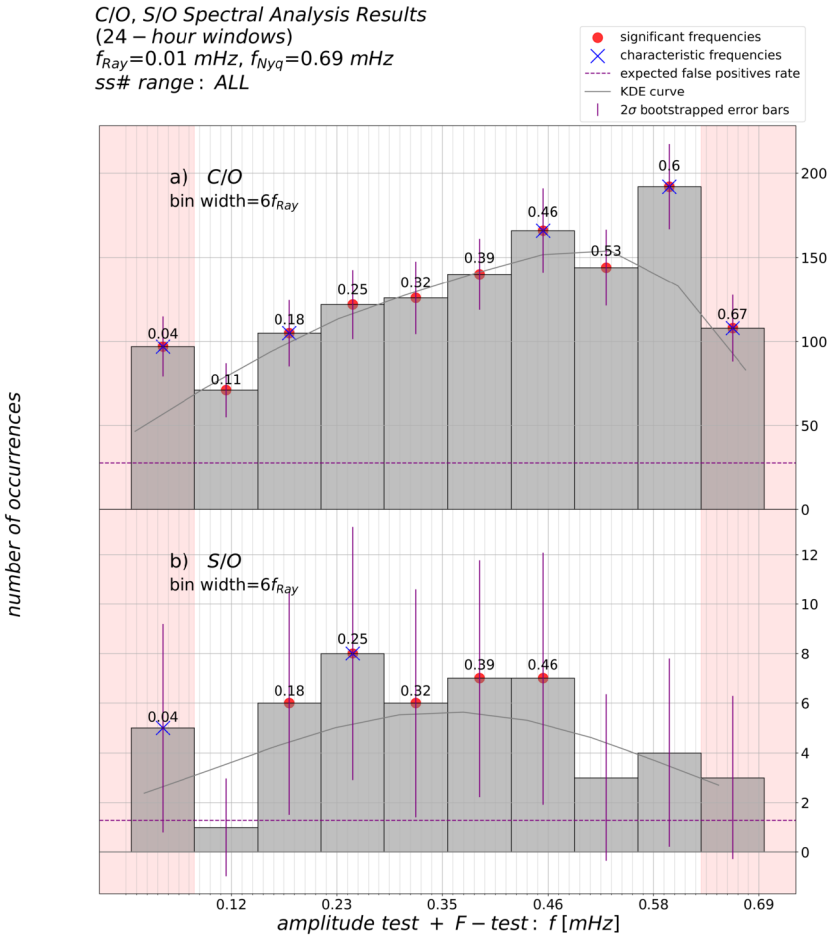

Figure 3 Periodic density structure occurrence distributions for the intermediate-FIP composition ratios (C/O and S/O). Error bars showing 2σ of the bootstrapped distributions are plotted as solid purple vertical lines. The occurrence distributions are shown in gray, and the expected false-positive rate for the method is shown as a dotted purple horizontal line. Significant frequencies are defined to rise $\geq 2\sigma$ above the expected false-positive rate. These are marked on the plot by red dots and the numerical value of the corresponding bin center. Characteristic frequencies are defined to rise $\geq 1\sigma$ above the gray KDE curve and are marked with a blue "x". The "extreme" low- and high-frequency ranges, shaded in red on each plot, indicate frequency bins prone to false positives, according to Monte-Carlo simulations (Di Matteo, Viall, and Kepko, 2021), and are therefore not considered statistically significant results.

the false positives rate) ranges from $\sim 0.2-0.6$ mHz (corresponding to approximately 30-minute to 90-minute periodicities). The 0.6 mHz enhancement is considered to be a characteristic scale in this distribution. Figure 3 shows distributions for C/O and S/O, the intermediate-FIP abundances. The S/O ratio has too few results to be considered robust, as it has bootstrapped 2σ error bars that are comparable in size to the number of occurrences in each bin, though the 0.25 mHz signal may be substantial. The C/O distribution rises steadily in an almost linear way with frequency. It has a broader range of statistically significant frequencies than the He/O distribution, spanning the entire frequency range under consid-

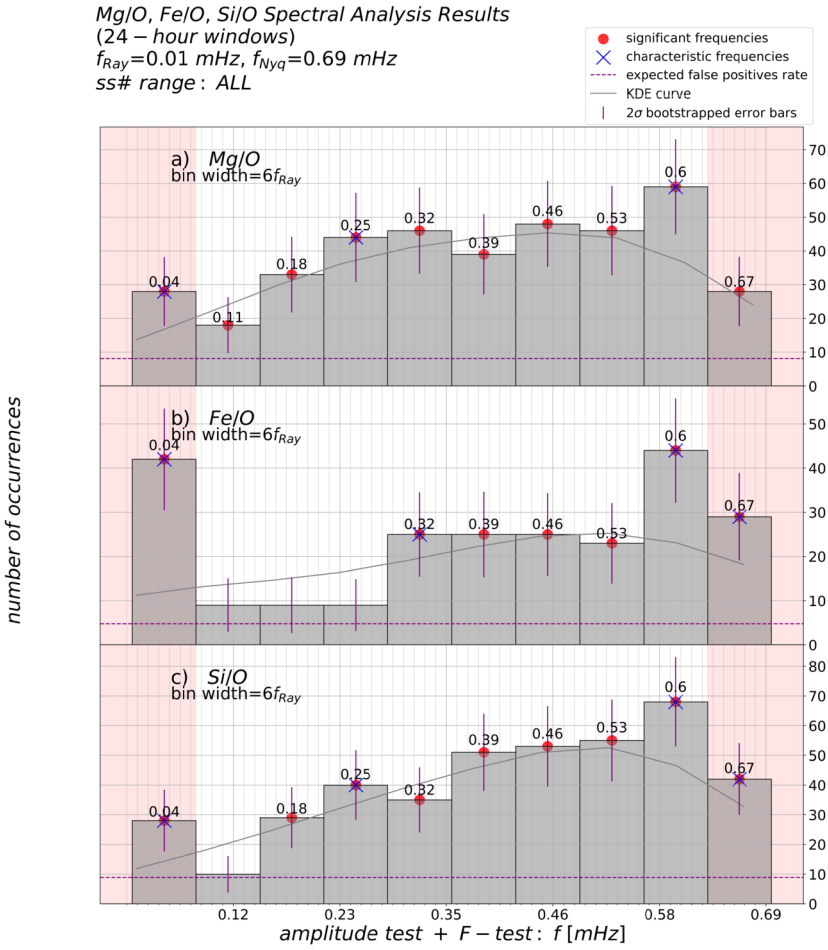

Figure 4 Periodic density structure occurrence distributions for the low-FIP composition ratios (Mg/O, Fe/O, and Si/O). Error bars showing 2σ of the bootstrapped distributions are plotted as solid purple vertical lines. The occurrence distributions are shown in gray, and the expected false-positive rate for the method is shown as a dotted purple horizontal line. Significant frequencies are defined to rise $\geq 2\sigma$ above the expected false-positive rate. These are marked on the plot by red dots and the numerical value of the corresponding bin center. Characteristic frequencies are defined to rise $\geq 1\sigma$ above the gray KDE curve and are marked with a blue "x". The extreme low- and high-frequency ranges, shaded in red on each plot, indicate frequency bins prone to false positives, according to Monte-Carlo simulations (Di Matteo, Viall, and Kepko, 2021), and are therefore not considered statistically significant results.

eration: $\sim 0.1 - 0.6$ mHz. Figure 4 shows the Mg/O, Fe/O, and Si/O low-FIP distributions, which, like the C/O intermediate-FIP distribution, also seem to rise linearly with frequency. Mg/O and Si/O have a wide, continuous range of significant frequencies, while the significant frequencies of the Fe/O distribution are concentrated above 0.3 mHz. The charge state ratios, shown in Figure 5, have similar shapes to the low-FIP and intermediate-FIP distributions and a similar range of statistically significant frequencies. The oxygen charge state distribution is very similar to the low-FIP ratio distributions in both shape and bin counts.

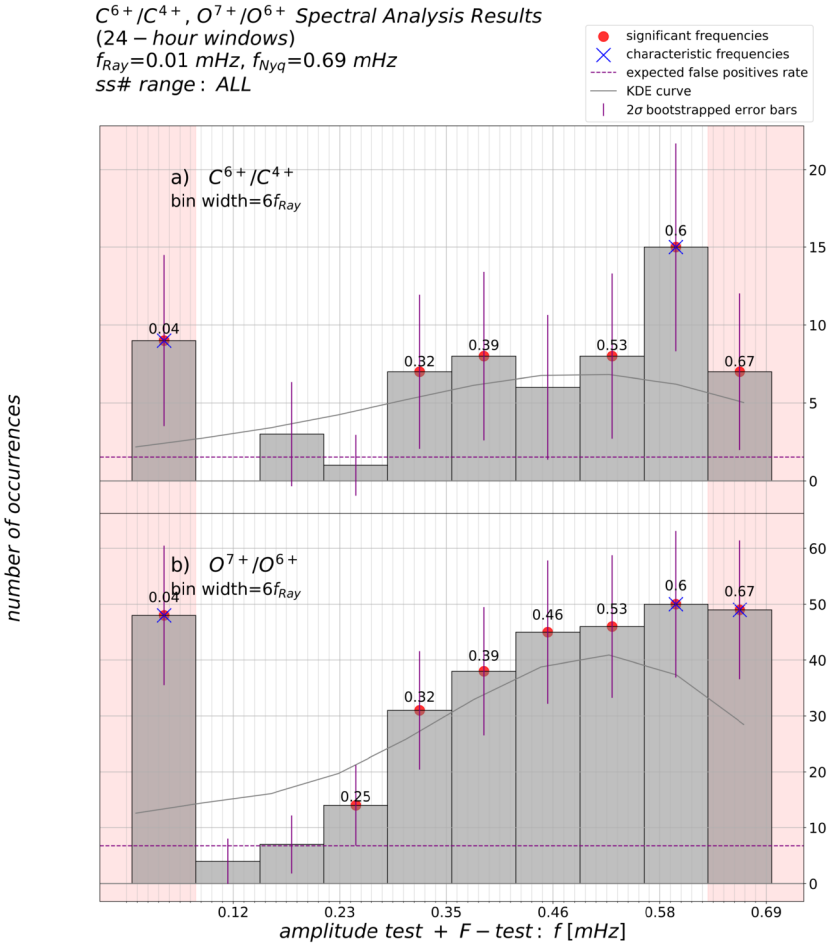

Figure 5 Periodic density structure occurrence distributions for the charge-state ratios (C^{6+}/C^{4+}, and O^{7+}/O^{6+}). Error bars showing 2σ of the bootstrapped distributions are plotted as solid purple vertical lines. The occurrence distributions are shown in gray, and the expected false-positive rate for the method is shown as a dotted purple horizontal line. Significant frequencies are defined to rise $\geq 2\sigma$ above the expected false-positive rate. These are marked on the plot by red dots and the numerical value of the corresponding bin center. Characteristic frequencies are defined to rise $\geq 1\sigma$ above the gray KDE curve and are marked with a blue "x". The extreme low- and high-frequency ranges, shaded in red on each plot, indicate frequency bins prone to false positives, according to Monte-Carlo simulations (Di Matteo, Viall, and Kepko, 2021), and are therefore not considered statistically significant results.

The carbon charge-state ratio distribution is sparse and the bootstrapped 2σ error bars indicate a high degree of uncertainty.

It can be seen that all abundance ratios with adequate statistics contain significant frequency ranges that rise well above the expected false-positives rate of our method. A characteristic scale or scales can be seen for all abundance and charge state ratios, as blue x's indicating enhancements of 1σ of the bootstrapped distribution above the KDE curve for the distribution. The 0.5 – 0.6 mHz range tends to exhibit the most common enhancement for all abundance ratios.

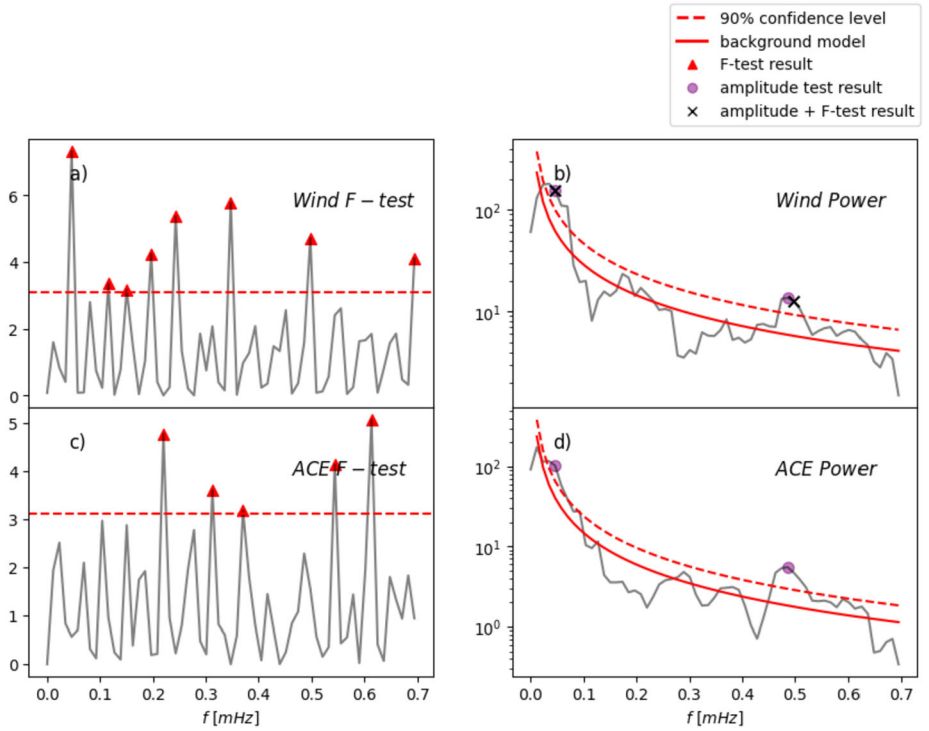

Figure 6 Spectral analysis results comparing ACE/SWICS to Wind/SWE He^{2+} spectra for the 24-hour period beginning on 2005-04-29 00:00:00 UT. Panels with the label "F-test" (a and c) show the F-test signals as red triangles above the dashed red 90% confidence level line. Panels labeled "Power" (b and d) show the estimated power spectral density in gray, the background fit as a solid red line, and the 90% confidence level as a dashed red curve. Results that passed the amplitude test are marked by purple circles. Results that pass both the amplitude and F-test are marked by a black "x". The 0.5 mHz peak passes the amplitude test at a 90% confidence level in both the ACE and Wind He^{2+} segments. The Wind segment also passes the F-test, which is used in support of the amplitude test.

3.2. Cross-Verification with Wind

While no other composition mass spectrometers similar to SWICS exist on other L1 monitors, we did take advantage of Wind having He abundance measurements in order to perform a comparison and verification. We have identified a time segment during which the ACE and the Wind spacecraft were observing the same parcel of solar wind and compared their He^{2+} spectra on the day of 29 April 2005. At the time of the observation, ACE and Wind were approximately 313,440 km apart. Figure 6 shows the specra from ACE/SWICS and the Wind Solar Wind Experiment (SWE). They have a similar shape in the upper frequency ranges (above 0.4 mHz), and show a distinct enhancement at $\sim$0.5 mHz, which matches a common enhancement in the occurrence distributions presented in Section 3.1.

3.3. Solar Activity Dependence

Figure 7 shows the average sunspot number for each of the 14 years considered in the study. For the purposes of this analysis, we categorized the solar activity by grouping years

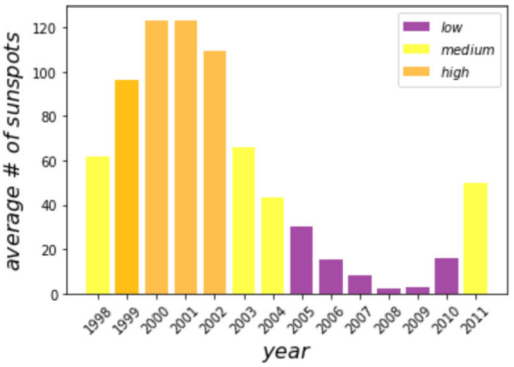

Figure 7 Solar activity during the 14 years of ACE/SWICS data analyzed (as measured by average yearly sunspot number).

with low (years 2005 – 2010), medium (years 1998, 2003, 2004, 2011), and high (years 1999 – 2002) average sunspot numbers and analyzed them within these categories. We also looked at the group of all years and analyzed the full 14-year dataset. Figure 8 shows the fraction of validated segments that contained one or more results for each ratio analyzed. From top panel to bottom panel, we show the result rate for the high-FIP ratio (He/O) in panel a), the intermediate-FIP ratios (S/O and C/O) in panel b), low-FIP ratios (Mg/O, Si/O, and Fe/O) in panel c), and charge-state ratios (C^{6+}/C^{4+} and O^{7+}/O^{6+}) in panel d). The y-axis in each panel shows the fraction of validated windows containing at least one result. The x-axis shows categories of average sunspot number: low, medium, high, and all years. The error bars represent one standard deviation and were generated from the bootstrapped distributions. This plot shows that the fraction of validated windows containing significant frequencies is fairly consistent (approximately 30% on average) for low, medium, and high solar activity levels (as measured by the average sunspot number for a given year), as has been reported for protons (Kepko, Viall, and Wolfinger, 2020).

4. Discussion

We have, for the first time, presented here occurrence distributions of statistically significant periodic structures identified in the elemental and charge state composition of the solar wind. As in the statistical studies of proton density structures in the solar wind (Kepko, Viall, and Wolfinger, 2020; Viall, Kepko, and Spence, 2008; Viall and Vourlidas, 2015), we see that periodic structures also exist at statistically significant levels in the elemental composition and charge state relative to the expected false-positive rate for our spectral analysis procedure (see Figures 2 – 5). The same figures also show that characteristic frequencies are present in most occurrence distributions (as evidenced by the peaks rising $\geq 1\sigma$ above the smoothed histograms). Mesoscale periodic structures, in general, are strongly associated with the formation and release of the solar wind. As discussed previously, periodic structures in elemental composition and charge states are particularly important tracers of these processes, as they are determined in the solar atmosphere and do not evolve en route to the observing instrument.

Figures 2 – 5 also show that the low-FIP, intermediate-FIP, and charge state distributions have a wider range of significant frequencies, typically extending to lower values, and exhibiting different shapes than the high-FIP (He/O) distribution. Among the low-FIP distributions, Fe/O stands out from Mg/O and Si/O in that, rather than exhibiting a wide, continuous range of statistically significant frequencies, it shows statistically significant frequency

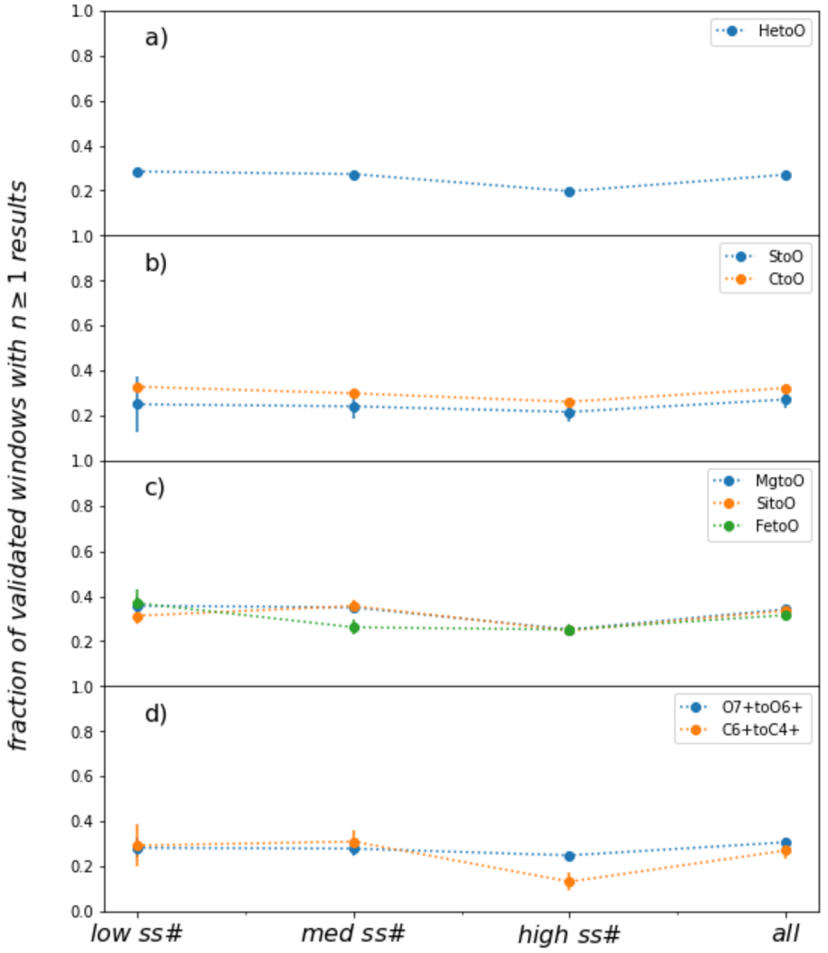

Figure 8 Solar cycle dependence of the fraction of validated windows that contained at least one statistically significant result passing both the harmonic F-test and amplitude test at a 90% confidence level. The result rates were fairly consistent throughout the solar cycle for all composition and charge-state abundances. The error bars represent 1σ of the bootstrapped distributions. The number of validated windows and results was low for the years corresponding to low solar activity, and thus, the error bars are large.

bands concentrated at the higher frequencies: $\sim 0.3-0.6$ mHz. The Mg/O and Si/O distributions look very similar to each other, and all three low-FIP distributions have a similar number of total results. The differences observed for Fe/O are likely due to gravitational settling, as Fe has a much higher mass than either Mg or Si. Gravitational setting in large, closed magnetic loops may introduce mass-dependent effects due to heavy ions sinking and lighter elements escaping first (Weberg, Zurbuchen, and Lepri, 2012).

Figure 9 shows a summary of the periodic structures identified for low-FIP, intermediate-FIP, high-FIP and charge state ratios. Significant frequencies are shown for the full dataset, as well as for high, medium, and low sunspot number year groupings. Statistically significant frequencies ($\geq 2\sigma$ above the expected false-positive rate line in Figures 2 – 5) are shown as empty circles. Characteristic frequencies ($\geq 1\sigma$ above the KDE curve for the distributions

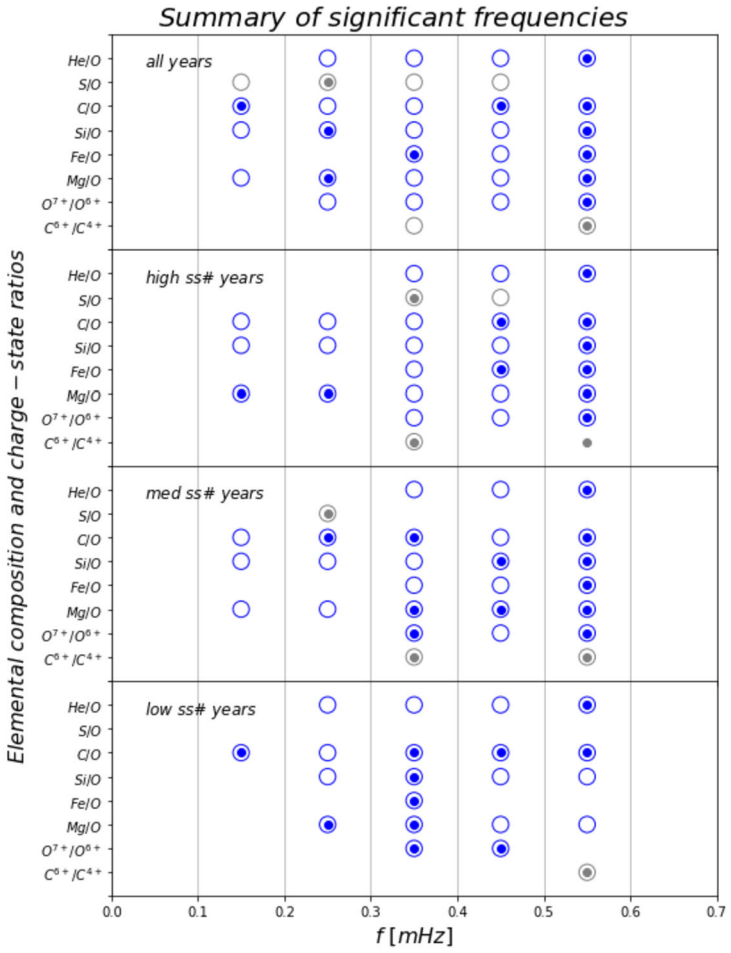

Figure 9 Summary of statistically significant (empty circles) and characteristic (filled circles) frequencies found for all elemental composition and charge-state ratios in the 14 years of ACE/SWICS data analyzed. Results are shown for the full data set, as well as for high, medium, and low sunspot number year groupings.

in Figures 2 – 5) are marked with filled circles. Results with large statistical uncertainty were grayed out. Though there was no strong dependence on solar activity in the number of validated windows with one or more results, the values of significant and characteristic frequencies did seem to exhibit some dependence. For example, the 0.25 mHz band is significant for He/O in low sunspot number years, but not for medium or high sunspot number year categories. Furthermore, the C/O abundance ratio exhibited the most characteristic frequencies (four) during the low sunspot number year category. This number declined for medium and high sunspot number year categories. He/O ratio exhibits a different shape from the other abundances, likely due to the fact that He is governed by different drivers than the other elements (Laming, 2015; Laming et al., 2019). The high-FIP (He/O) and intermediate-FIP (C/O) ratio significant frequencies were fairly stable for the four categories of solar activity. The low-FIP statistically significant results, however, are more variable. This is likely due

to the fact the He and C abundances are much more prevalent in the solar wind and that the statistics available for the heavier ions are marginal during periods of low solar activity.

In this study, we have only been able to cover the frequency range below 0.6 mHz, the lower band of frequencies examined in the proton density structure studies reported by Kepko, Viall, and Wolfinger (2020), Viall, Kepko, and Spence (2008). This is due to the fact that heavy ions are present in trace amounts in the solar wind and therefore require longer instrument accumulation times, and thus a lower temporal resolution, in order to acquire sufficient counts than do protons. Thus, we were only able to characterize the largest scales considered in the studies of proton periodic density structures.

The $\sim 0.5-0.6$ mHz frequency band (approximately 30 min or 720 Mm for a solar wind speed of 400 km s^{-1}) is a characteristic scale for several elemental composition ratios and also appears in the charge state. This is a result that has been reported about periodic mesoscale proton density structures as well as about magnetospheric oscillations (Kepko, Viall, and Wolfinger, 2020; Viall, Kepko, and Spence, 2009, 2008; Kepko and Spence, 2003; Lyons et al., 2002; Lessard et al., 2003). The Viall, Kepko, and Spence (2009) statistical study showed this band to be a characteristic range in the solar wind as well as being responsible for driving the magnetosphere. Furthermore, the Kepko and Spence (2003) event study identifies this as one of the frequency bands for which magnetic-field oscillations are observed to be directly driven by proton periodic density structures in the solar wind. Thus, this is an important frequency band for connecting solar wind observations to magnetospheric oscillations. The $\sim 0.5-0.6$ mHz frequency band was also identified in event studies of solar wind elemental composition and charge state Kepko et al. (2016), Gershkovich et al. (2022). Kepko, Spence, and Singer (2002) and Villante, Francia, and Lepidi (2001) report a 0.7 mHz frequency result with significant power in magnetic-field oscillations driven by proton periodic density structures and ground magnetometer data respectively. In our study, this frequency is limited by the Nyquist frequency of the ACE/SWICS data, but we do observe power in the frequency range ≥ 0.6 mHz in the composition data as well as the charge state.

The Viall and Vourlidas (2015) study of periodic proton density structures coming off of the Sun, observed in coronagraph data, was even more limited, with a Nyquist frequency of 0.3 mHz. This study found a characteristic frequency of ~ 0.2 mHz (approximately 90 min or 2160 Mm for a solar wind speed of 400 km s^{-1}) to be associated with the heliospheric current sheet (HCS), which is likely related to the 0.25 mHz result observed in this study. The modeling work reported by Réville et al. (2020) and Pylaev et al. (2017) predicted periodicities in this range at the HCS due to quasi-periodic reconnection occurring at the helmet streamer tips.

Multiple simulations modeling the reconnection processes at streamers in the solar corona and the associated time scales have been performed (Wyper and Jain, 2010; Lynch, Edmondson, and Li, 2014; Higginson and Lynch, 2018; Pylaev et al., 2017; Réville et al., 2020; Schlenker et al., 2021; Allred and MacNeice, 2015). When taken together, these simulation studies suggest that different observed frequencies within the solar wind can help characterize the details of the specific reconnection process responsible for the measured structures. In general, the mHz frequency range of our results suggests streamers as a likely source, with reconnection possibly being modulated by the oscillations in the structure as a whole. This frequency range (~ 1 mHz) is indicated by taking an Alfvén speed of 1.e8 cm s^{-1} and a length scale of 1.e11 cm. Pylaev et al. (2017), as discussed above, predict a reconnection frequency that is associated with the acoustic cutoff frequency, whereas Réville et al. (2020) attribute their results to the tearing instability – a process more intrinsic to the reconnection itself. Oscillations at ~ 1 mHz (and lower) appear to be present in the

magnetohydrodynamic modeling of thermal nonequilibrium in streamers by Schlenker et al. (2021), suggesting a slightly different process modulating the reconnection than proposed by either Pylaev et al. (2017) or Réville et al. (2020). Lastly, the model of interchange reconnection proposed by Lynch, Edmondson, and Li (2014) has a characteristic timescale close to 2.e3 s, corresponding to a ~ 0.5 mHz frequency, which is similar to the global Alfvén frequency. This too suggests that a slightly different mechanism may be responsible from those previously cited and that these differences can help link observed structures to the processes that produced them.

We have divided the 1998–2011 ACE/SWICS data into segments consisting of several years each, characterized by average sunspot number, in order to study the impact of solar activity on the number and types of periodic structures observed. Figure 8 shows the fraction of validated segments, which contained one or more significant periodicities for the elemental abundance ratios and charge states in the study. The figure indicates that the result rates are fairly constant for low, medium, and high average sunspot-numbered year groupings, as well as when all years are analyzed together. This is consistent with what was observed by Kepko, Viall, and Wolfinger (2020) in the study of proton periodic density structures and their dependence on solar activity.

We have also identified a time period during which ACE/SWICS and Wind/SWE were observing the same parcel of solar wind. Their He^{2+} spectra are highly similar, exhibiting the same enhancements and depletions in power, especially in the higher-frequency bins (≥ 0.4 mHz). They share a 0.5 mHz enhancement identified by our spectral analysis procedure for both instruments. Several elemental abundance ratios and charge state occurrence distributions contain a characteristic scale in the $0.5-0.6$ mHz range that matches this result. This cross-validation sets a lower limit on the spatial scale over which the structures were highly coherent, as the spacecraft were over 300,000 km apart during this segment, and rules out instrumental effects as being responsible for the periodic structure observed.

5. Conclusion

In this work, we have expanded upon previously conducted statistical studies of solar wind periodic density structures by extending the analysis from proton data to high-resolution elemental composition and charge-state measurements. Variations in composition are an important tool for understanding how the solar wind connects to its sources on the Sun, how it is formed, and how it is released. This is because composition is established at the Sun and cannot evolve en route to the point of observation. We have provided occurrence distributions of statistically significant periodic structures found in low-FIP, intermediate-FIP, high-FIP, and charge state abundance ratios, and showed that there is a characteristic scale, as some frequencies occur more often than others throughout the 14 years. Significant and characteristic enhancements were observed at a level substantially above the false-positive rate of our spectral analysis method. We show that the width of the statistically significant frequency bands for each distribution is dependent on FIP and that the Fe/O distribution differs substantially from the other low-FIP ratio distributions (Mg/O and Si/O), likely due to gravitational settling effects dominating the heavy Fe ions in some solar processes (Weberg, Zurbuchen, and Lepri, 2012). The $\sim 0.5-0.6$ mHz characteristic scale found to be prevalent in this study is associated with observations of magnetospheric oscillations that were previously linked to proton density structures in the solar wind. It has also been observed in statistical studies of proton density structures (Kepko, Viall, and Wolfinger, 2020) and in an event study by Viall, Spence, and Kasper (2009). The 0.25 mHz result supports the coronagraph studies of

Viall and Vourlidas (2015), which identified a 0.2 mHz characteristic scale associated with the HCS, as well as confirms the predictions of Réville et al. (2020), Pylaev et al. (2017).

In line with the proton statistical study findings of Kepko, Viall, and Wolfinger (2020), we have determined that the number of validated windows for all ratios considered in the analysis, containing at least one result, does not exhibit a dependence on solar activity. The values of the significant and characteristic frequencies, however, do exhibit a dependence on solar activity, as measured by the yearly averaged sunspot number. This is also in line with what was reported by Kepko, Viall, and Wolfinger (2020). Finally, we have identified a time segment during which the ACE/SWICS and Wind/SWE instruments were observing the same parcel of solar wind and during which their He^{2+} number density data exhibited matching spectra with a distinct enhancement at ~ 0.5 mHz, a significant frequency for several distributions presented in this study.

Future work will be to apply the methods and techniques presented here to higher-resolution data sets, covering observations from a large range of orbital distances, measured by new instruments such as Solar Orbiter's Heavy Ion Sensor.

Author contributions I.G. wrote the main manuscript text and prepared the figures. All authors contributed to and reviewed the manuscript.

Funding The work by all authors was supported by the NASA competed Heliophysics Internal Scientist Funding Model. IG and STL were supported as a subcontract of this program with award number 80NSSC20K1063. SDM was supported under the NASA Grant 80NSSC21K0459.

Data Availability Supporting solar wind observations from ACE are available on the ACE Science Center website at http://www.srl.caltech.edu/ace/ASC/. The 12-minute ACE/SWICS dataset was processed and provided by the University of Michigan.

Declarations

Competing interests The authors declare no competing interests.

References

Allred, J., MacNeice, P.: 2015, An mhd code for the study of magnetic structures in the solar wind. *Comput. Sci. Discov.* **8**(1), 015002.

Antiochos, S., Mikić, Z., Titov, V., Lionello, R., Linker, J.: 2011, A model for the sources of the slow solar wind. *Astrophys. J.* **731**(2), 112.

Borovsky, J.E.: 2008, Flux tube texture of the solar wind: strands of the magnetic carpet at 1 AU? *J. Geophys. Res. (Space Phys.)* **113**(A8), A08110.

Crooker, N., Gosling, J., Kahler, S.: 2002, Reducing heliospheric magnetic flux from coronal mass ejections without disconnection. *J. Geophys. Res. (Space Phys.)* **107**(A2), 1028.

DeForest, C., Matthaeus, W., Viall, N., Cranmer, S.: 2016, Fading coronal structure and the onset of turbulence in the young solar wind. *Astrophys. J.* **828**(2), 66.

DeForest, C., Howard, R.A., Velli, M., Viall, N., Vourlidas, A.: 2018, The highly structured outer solar corona. *Astrophys. J.* **862**(1), 18.

Di Matteo, S., Viall, N.M., Kepko, L.: 2021, Power spectral density background estimate and signal detection via the multitaper method. *J. Geophys. Res. (Space Phys.)* **126**, e28748.

Di Matteo, S., Viall, N., Kepko, L., Wallace, S., Arge, C., MacNeice, P.: 2019, Helios observations of quasiperiodic density structures in the slow solar wind at 0.3, 0.4, and 0.6 AU. *J. Geophys. Res. (Space Phys.)* **124**(2), 837.

Dyrud, L., Behnke, R., Kepko, E., Sulzer, M., Zafke, S.: 2008, Ionospheric ULF oscillations driven from above arecibo. *Geophys. Res. Lett.* **35**(14), L14101.

Efron, B., Tibshirani, R.J.: 1994, *An Introduction to the Bootstrap*, CRC Press, Boca Raton.

Fenrich, F., Waters, C.: 2008, Phase coherence analysis of a field line resonance and solar wind oscillation. *Geophys. Res. Lett.* **35**(20), L20102.

Fisk, L.: 2003, Acceleration of the solar wind as a result of the reconnection of open magnetic flux with coronal loops. *J. Geophys. Res. (Space Phys.)* **108**(A4), 1157.

Geiss, J., Gloeckler, G., Fisk, L., Von Steiger, R.: 1995, C+ pickup ions in the heliosphere and their origin. *J. Geophys. Res. (Space Phys.)* **100**(A12), 23373.

Gershkovich, I., Lepri, S.T., Viall, N.M., Di Matteo, S., Kepko, L.: 2022, Periodic solar wind structures observed in measurements of elemental and ionic composition in situ at L1. *Astrophys. J.* **933**(2), 198.

Gloeckler, G., Zurbuchen, T.H., Geiss, J.: 2003, Implications of the observed anticorrelation between solar wind speed and coronal electron temperature. *J. Geophys. Res. (Space Phys.)* **108**(A4), 1158.

Gloeckler, G., Galvin, A., Ipavich, F., Geiss, J., Balsiger, H., von Steiger, R., Fisk, L., Ogilvie, K., Wilken, B.: 1993, Detection of interstellar pick-up hydrogen in the solar system. *Science* **261**(5117), 70.

Gloeckler, G., Cain, J., Ipavich, F., Tums, E., Bedini, P., Fisk, L., Zurbuchen, T., Bochsler, P., Fischer, J., Wimmer-Schweingruber, R., et al.: 1998, *Investigation of the Composition of Solar and Interstellar Matter Using Solar Wind and Pickup Ion Measurements with SWICS and SWIMS on the ACE Spacecraft*, Springer, Berlin.

Gloeckler, G., Fisk, L., Geiss, J., Schwadron, N., Zurbuchen, T.: 2000, Elemental composition of the inner source pickup ions. *J. Geophys. Res. (Space Phys.)* **105**(A4), 7459.

Gloeckler, G., Geiss, J., Balsiger, H., Bedini, P., Cain, J., Fischer, J., Fisk, L., Galvin, A., Gliem, F., Hamilton, D., et al.: 1992, The solar wind ion composition spectrometer. *Astronomy and Astrophysics Supplement Series* **92**, 267.

Higginson, A.K., Lynch, B.J.: 2018, Structured slow solar wind variability: streamer-blob flux ropes and torsional Alfvén waves. *Astrophys. J.* **859**(1), 6.

Hundhausen, A., Gilbert, H., Bame, S.: 1968, Ionization state of the interplanetary plasma. *J. Geophys. Res.* **73**(17), 5485.

Kepko, L., Spence, H.E.: 2003, Observations of discrete, global magnetospheric oscillations directly driven by solar wind density variations. *J. Geophys. Res. (Space Phys.)* **108**(A6), 1257.

Kepko, L., Spence, H.E., Singer, H.: 2002, Ulf waves in the solar wind as direct drivers of magnetospheric pulsations. *Geophys. Res. Lett.* **29**(8), 39.

Kepko, L., Viall, N.M., Wolfinger, K.: 2020, Inherent length scales of periodic mesoscale density structures in the solar wind over two solar cycles. *J. Geophys. Res. (Space Phys.)* **125**(8), e28037.

Kepko, L., Viall, N., Antiochos, S., Lepri, S., Kasper, J., Weberg, M.: 2016, Implications of L1 observations for slow solar wind formation by solar reconnection. *Geophys. Res. Lett.* **43**(9), 4089.

Kilpua, E., Koskinen, H.E., Pulkkinen, T.I.: 2017, Coronal mass ejections and their sheath regions in interplanetary space. *Living Rev. Solar Phys.* **14**(1), 5.

Laming, J.M.: 2015, The FIP and inverse FIP effects in solar and stellar coronae. *Living Rev. Solar Phys.* **12**, 2.

Laming, J.M., Vourlidas, A., Korendyke, C., Chua, D., Cranmer, S.R., Ko, Y.-K., Kuroda, N., Provornikova, E., Raymond, J.C., Raouafi, N.-E., et al.: 2019, Element abundances: a new diagnostic for the solar wind. *Astrophys. J.* **879**(2), 124.

Landi, E., Gruesbeck, J., Lepri, S.T., Zurbuchen, T.H., Fisk, L.: 2012, Charge state evolution in the solar wind. II. Plasma charge state composition in the inner corona and accelerating fast solar wind. *Astrophys. J.* **761**(1), 48.

Lessard, M., Hanna, J., Donovan, E., Reeves, G.: 2003, Evidence for a discrete spectrum of persistent magnetospheric fluctuations below 1 mHz. *J. Geophys. Res. (Space Phys.)* **108**(A3), 1125.

Lynch, B., Edmondson, J., Li, Y.: 2014, Interchange reconnection Alfvén wave generation. *Solar Physics* **289**, 3043.

Lyons, L., Zesta, E., Xu, Y., Sánchez, E., Samson, J., Reeves, G., Ruohoniemi, J., Sigwarth, J.: 2002, Auroral poleward boundary intensifications and tail bursty flows: a manifestation of a large-scale ULF oscillation? *J. Geophys. Res. (Space Phys.)* **107**(A11), 1352.

Murphy, A.K., Winslow, R.M., Schwadron, N.A., Lugaz, N., Yu, W., Farrugia, C.J., Niehof, J.T.: 2020, A survey of interplanetary small flux ropes at Mercury. *Astrophys. J.* **894**(2), 120.

Ogilvie, K., Bochsler, P., Geiss, J., Coplan, M.: 1980, Observations of the velocity distribution of solar wind ions. *J. Geophys. Res. (Space Phys.)* **85**(A11), 6069.
Pylaev, O., Zaqarashvili, T., Brazhenko, A., Melnik, V., Hanslmeier, A., Panchenko, M.: 2017, Oscillation of solar radio emission at coronal acoustic cut-off frequency. *Astron. Astrophys.* **601**, A42.
Réville, V., Velli, M., Rouillard, A.P., Lavraud, B., Tenerani, A., Shi, C., Strugarek, A.: 2020, Tearing instability and periodic density perturbations in the slow solar wind. *Astrophys. J. Lett.* **895**(1), L20.
Richardson, I.G.: 2018, Solar wind stream interaction regions throughout the heliosphere. *Living Rev. Solar Phys.* **15**(1), 1.
Rouillard, A., Davies, J., Lavraud, B., Forsyth, R., Savani, N., Bewsher, D., Brown, D.S., Sheeley, N., Davis, C., Harrison, R., et al.: 2010, Intermittent release of transients in the slow solar wind: 1. Remote sensing observations. *J. Geophys. Res. (Space Phys.)* **115**(A4), A04103.
Rouillard, A.P., Kouloumvakos, A., Vourlidas, A., Kasper, J., Bale, S., Raouafi, N.-E., Lavraud, B., Howard, R.A., Stenborg, G., Stevens, M., et al.: 2020, Relating streamer flows to density and magnetic structures at the Parker solar probe. *Astrophys. J. Suppl.* **246**(2), 37.
Sanchez-Diaz, E., Rouillard, A., Lavraud, B., Kilpua, E., Davies, J.: 2019, In situ measurements of the variable slow solar wind near sector boundaries. *Astrophys. J.* **882**(1), 51.
Schlenker, M.J., Antiochos, S.K., MacNeice, P.J., Mason, E.I.: 2021, The effect of thermal nonequilibrium on helmet streamers. *Astrophys. J.* **916**(2), 115.
Scott, D.W.: 2015, *Multivariate Density Estimation: Theory, Practice, and Visualization*, Wiley, New York.
Shearer, P., von Steiger, R., Raines, J.M., Lepri, S.T., Thomas, J.W., Gilbert, J.A., Landi, E., Zurbuchen, T.H.: 2014, The solar wind neon abundance observed with ACE/SWICS and Ulysses/SWICS. *Astrophys. J.* **789**(1), 60.
Slepian, D.: 1978, Prolate spheroidal wave functions, Fourier analysis, and uncertainty—V: the discrete case. *Bell Syst. Tech. J.* **57**(5), 1371.
Stakhiv, M., Landi, E., Lepri, S.T., Oran, R., Zurbuchen, T.H.: 2015, On the origin of mid-latitude fast wind: challenging the two-state solar wind paradigm. *Astrophys. J.* **801**(2), 100.
Stansby, D., Horbury, T.: 2018, Number density structures in the inner heliosphere. *Astron. Astrophys.* **613**, A62.
Thomson, D.J.: 1982, Spectrum estimation and harmonic analysis. *Proc. IEEE* **70**(9), 1055.
Verscharen, D., Klein, K.G., Maruca, B.A.: 2019, *The Multi-Scale Nature of the Solar Wind*, Springer, Berlin.
Viall, N.M., Borovsky, J.E.: 2020, Nine outstanding questions of solar wind physics. *J. Geophys. Res. (Space Phys.)* **125**(7), e26005.
Viall, N., DeForest, C., Kepko, L.: 2021, Mesoscale structure in the solar wind. *Front. Astron. Space Sci.* **139**, 735034.
Viall, N., Kepko, L., Spence, H.E.: 2008, Inherent length-scales of periodic solar wind number density structures. *J. Geophys. Res. (Space Phys.)* **113**(A7), A07101.
Viall, N., Kepko, L., Spence, H.E.: 2009, Relative occurrence rates and connection of discrete frequency oscillations in the solar wind density and dayside magnetosphere. *J. Geophys. Res. (Space Phys.)* **114**, A01201.
Viall, N.M., Spence, H.E., Kasper, J.: 2009, Are periodic solar wind number density structures formed in the solar corona? *Geophys. Res. Lett.* **36**(23), L23102.
Viall, N.M., Vourlidas, A.: 2015, Periodic density structures and the origin of the slow solar wind. *Astrophys. J.* **807**(2), 176.
Viall, N.M., Spence, H.E., Vourlidas, A., Howard, R.: 2010, Examining periodic solar-wind density structures observed in the SECCHI heliospheric imagers. *Solar Phys.* **267**(1), 175.
Villante, U., Di Matteo, S., Piersanti, M.: 2016, On the transmission of waves at discrete frequencies from the solar wind to the magnetosphere and ground: a case study. *J. Geophys. Res. (Space Phys.)* **121**(1), 380.
Villante, U., Francia, P., Lepidi, S.: 2001, Pc5 geomagnetic field fluctuations at discrete frequencies at a low latitude station. *Annales Geophysicae* **19**, 321.
Villante, U., Francia, P., Vellante, M., Di Giuseppe, P., Nubile, A., Piersanti, M.: 2007, Long-period oscillations at discrete frequencies: a comparative analysis of ground, magnetospheric, and interplanetary observations. *J. Geophys. Res. (Space Phys.)* **112**(A4), A04210.
Von Steiger, R., Schwadron, N., Fisk, L., Geiss, J., Gloeckler, G., Hefti, S., Wilken, B., Wimmer-Schweingruber, R., Zurbuchen, T.: 2000, Composition of quasi-stationary solar wind flows from Ulysses/solar wind ion composition spectrometer. *J. Geophys. Res. (Space Phys.)* **105**(A12), 27217.
Weberg, M.J., Zurbuchen, T.H., Lepri, S.T.: 2012, ACE/SWICS observations of heavy ion dropouts within the solar wind. *Astrophys. J.* **760**(1), 30.
Winterhalter, D., Neugebauer, M., Goldstein, B.E., Smith, E.J., Bame, S.J., Balogh, A.: 1994, Ulysses field and plasma observations of magnetic holes in the solar wind and their relation to mirror-mode structures. *J. Geophys. Res.* **99**(A12), 23371.
Wyper, P., Jain, R.: 2010, Torsional magnetic reconnection at three dimensional null points: a phenomenological study. *Phys. Plasmas* **17**(9), 092902.